symmetry

MDPI

Article

Symmetric versus Asymmetric Features of Homologous Homodimeric Amine Oxidases: When Water and Cavities Make the Difference

Eleonora Nicolai [1,†], Velia Minicozzi [2,†], Luisa Di Paola [3], Rosaria Medda [4], Francesca Pintus [4], Giampiero Mei [1,*] and Almerinda Di Venere [1,*]

[1] Department of Experimental Medicine, Tor Vergata University of Rome, Via Montpellier 1, 00133 Rome, Italy; nicolai@med.uniroma2.it
[2] Department of Physics, Tor Vergata University of Rome, Via della Ricerca Scientifica 1, 00133 Rome, Italy; velia.minicozzi@roma2.infn.it
[3] Unit of Chemical-Physics Fundamentals in Chemical Engineering, Department of Engineering, University Campus Bio-Medico of Rome, Via Álvaro del Portillo 21, 00128 Rome, Italy; l.dipaola@unicampus.it
[4] Department of Sciences of Life and Environment, University of Cagliari, 09124 Cagliari, Italy; rmedda@unica.it (R.M.); fpintus@unica.it (F.P.)
* Correspondence: mei@med.uniroma2.it (G.M.); divenere@med.uniroma2.it (A.D.V.)
† These authors contributed equally to this work.

Abstract: Symmetry is an intrinsic property of homo-oligomers. Amine oxidases are multidomain homodimeric enzymes that contain one catalytic site per subunit, and that share a high homology degree. In this paper, we investigated, by fluorescence spectroscopy measurements, the conformational dynamics and resiliency in solutions of two amine oxidases, one from lentil seedlings, and one from *Euphorbia characias* latex, of which the crystallographic structure is still unknown. The data demonstrate that slight but significant differences exist at the level of the local tridimensional structure, which arise from the presence of large internal cavities, which are characterized by different hydration extents. Molecular dynamics and a contact network methodology were also used to further explore, in silico, the structural features of the two proteins. The analysis demonstrates that the two proteins show similar long-range symmetrical connectivities, but that they differ in their local (intra-subunit) contact networks, which appear mostly asymmetric. These features have been interpreted to suggest a new rationale for the functioning of amino oxidases as obligate homodimers.

Keywords: amine oxidases; protein asymmetry; cluster analysis; dynamic fluorescence

Citation: Nicolai, E.; Minicozzi, V.; Di Paola, L.; Medda, R.; Pintus, F.; Mei, G.; Di Venere, A. Symmetric versus Asymmetric Features of Homologous Homodimeric Amine Oxidases: When Water and Cavities Make the Difference. *Symmetry* **2022**, *14*, 522. https://doi.org/10.3390/sym14030522

Academic Editor: Jesús F. Arteaga

Received: 30 January 2022
Accepted: 25 February 2022
Published: 3 March 2022

1. Introduction

The world of oligomers is dominated by proteins that are formed by identical subunits [1]. This feature provides these macromolecules with a high degree of spatial symmetry, which is a quality that strongly influences both their structural and functional properties, and that confers on them several advantages, such as stability, allosteric regulation, and protection from the risk of aggregation [2]. An accurate study on the protein complexes that are present in the Protein Data Bank has demonstrated that the vast majority of oligomers are symmetric homomers that are prevalently formed by an even number of identical subunits [3]. Protein–protein interaction and association are favored by structural similarity [4] because symmetric interfaces are, in general, energetically favored with respect to heterologous interfaces [1]. Despite the advantages conferred by a symmetric organization, an analysis of the protein crystallographic database revealed that examples of asymmetric structures also exist, and that asymmetry possibly plays an important role in cell biology [5]. At variance with global asymmetry, which is scarcely encountered in the world of homomers [5], local asymmetric arrangements are more frequent, and they arise

from the dynamic conformational changes that are induced by side-chain interactions and movements [2]. Interestingly, evolution has privileged the homomers that are characterized by a cyclic symmetry, and especially, among them, dimers with twofold symmetry axes [1,3,6]. Copper/TPQ-containing amine oxidases (AOs) are ubiquitous homodimeric enzymes that belong to this group, and they contain, in the active site of each monomer, one copper ion, and a 2,4,5-trihydroxyphenylalanine quinone (namely, TPQ) as a cofactor, which is derived from the post-translational oxidation of a tyrosine residue that is inserted in the highly conserved sequence (Asn-Tyr-Asp/Glu). Their biological function consists of the oxidative deamination of mono-, di- and polyamines, but they are also indirectly involved in a number of important cellular processes through the activity of their reaction products. In plants, two classes of amine oxidases have been identified, namely, copper- (CuAOs) and FAD-dependent AOs, both of which are implicated in cell-wall structural changes, in differentiation, and in programmed cell death [7]. The best-characterized copper/TPQ AOs from plants are those of *Pisum sativum* (PSAO), *Lens esculenta* (lentil seedling amine oxidase (LSAO)), and *Euphorbia characias* (Euphorbia latex amine oxidase (ELAO)). The three enzymes share about 86% sequence identity, and a similar molecular mass of about 145 kDa. Among them, only PSAO has been crystallized and characterized by single-crystal X-ray diffraction [8]. The PSAO dimer has a mushroom-like shape, where each subunit consists of three topological domains, namely, D2, D3, and D4. The active sites are buried in a funnel-shaped cavity that is located in the largest D4 domains, which form the interface of the dimer. The subunits are also held together by two β-hairpin arms, I and II, which extend from one D4 domain to wrap around the D4 domain of the other subunit. Such a peculiar arrangement gives rise to a very extended and complex monomer–monomer interface. The structures of the LSAO and ELAO have been analyzed by small-angle X-ray scattering, which shows that they share the same topology and that they closely resemble the crystal structure of PSAO [9]. However, in solution, these proteins seem to have a specific flexible region, and, in particular, the D3 domain could result in a conformational change, which increases the accessibility of the active site. In this study, we have analyzed the conformational dynamics and flexibility of LSAO and ELAO by fluorescence spectroscopy at atmospheric and high (≈2500 bar) pressure. Furthermore, molecular dynamics was used to estimate the possible three-dimensional configuration of both proteins by using the crystallographic coordinates of the PSAO as a template. The results indicate that the two proteins undergo different conformational dynamics, the features of which are mainly dictated by the presence of three large internal cavities, whose hydration states are greater in the case of the LSAO. We also discussed these findings in the light of the topological analysis of the simulated structures, which demonstrate how the presence of water enhances the degree of connectivity among the residues populating the subunit interface.

2. Materials and Methods

2.1. Enzymes

Amine oxidases from lentil (*Lens esculenta*) seedlings and from *E. characias* latex were purified as previously reported [9]. The purified enzymes were exhaustively dialyzed against a 50 mM Tris-HCl buffer, with a pH of 7.0. For each experiment, the proteins were appropriately diluted, and the concentration was determined using an ε_{498} of 4100 M^{-1} cm^{-1} for the LSAO, and an ε_{496} of 6000 M^{-1} cm^{-1} for the ELAO [9].

2.2. Fluorescence Assays

Steady-state fluorescence pressure measurements were performed with an ISS-K2 fluorometer (ISS, Champaign, IL, USA), and the temperatures of the samples were maintained by an external bath circulator.

In particular, the ANS binding to the ELAO or the LSAO (concentration ratio: 10:1) was studied by measuring the fluorescence emission spectra from 450 to 550 nm of the probe,

using an excitation wavelength of 350 nm, while the high-pressure protein fluorescence spectra were recorded using the ISS high-pressure cell (λ_{exc} = 293 nm, λ_{em} = 300–450).

The center of mass of the fluorescence steady-state emission spectra was fitted according to a two-state model, because the transition was dependent on the protein concentration, according to the scheme:

$$D_2 \leftrightarrow 2M \leftrightarrow 2M*$$

where D_2 is the folded dimer, and M and M* are the folded and partially unfolded monomeric species, respectively.

An estimation of the free energy and the partial molar volume change that was obtained at each transition was obtained using the relationship [10]:

$$K = e^{\frac{-\Delta G_0 + \Delta V[P]}{RT}}$$

Lifetime and dynamic fluorescence anisotropies were performed using the phase-shift demodulation technique on a KOALA-ISS fluorimeter (ISS, Champaign, IL, USA). The excitation source was a 300 nm laser diode, and the emission was collected through a WG320 nm cutoff filter to avoid scattering. The fluorescence emission decay was fitted accordingly to a Lorentzian continuously distributed model with three components, according to:

$$f(t) = \int_0^\infty F_i(\tau) e^{\frac{-t}{\tau}} d(\tau) \qquad \text{with} \qquad F_i(\tau) = \frac{\left(\frac{w_i}{2}\right)^2}{(\tau - \tau_i)^2 + \left(\frac{w_i}{2}\right)^2}$$

where i = 1, 2, and 3; and $F_i(\tau)$, τ_i, and w_i represent the fluorescence fractional intensity, the lifetime value, and the full width at half maximum (FWHM) of each component, respectively.

The anisotropy decays were collected through Glan–Thompson polarizers, taking into account the G-factor correction. All the measurements were repeated in triplicate to obtain a good statistic. The data were analyzed with the software provided by ISS accounting for the relative fluorescence lifetimes.

2.3. Molecular Graphics and Cavity Detection

All of the molecular graphics representations were obtained through VMD (Visual Molecular Dynamics) software version 1.9.3 [11]. The search for internal cavities was performed using two different routines, namely, 3D-Surfer [12], and POCASA [13], by using the structures at 25 °C that were obtained by the dynamic simulations at 20 ns and 30 ns for the LSAO and the ELAO, respectively.

2.4. Molecular Dynamics and Contact Network Analysis

Classical MD simulations of the PSAO, the LSAO, and the ELAO proteins were performed by employing the GROMACS package [14] with a CHARMM27 force field [15]. The starting structures for the three proteins are the ones considered by Dainese and co-workers [9]. The simulations were carried out in the NPT ensemble at 25 and 40 °C, and by employing the v-rescale thermostat [16], with a coupling time of 0.1 ps. The pressure was kept constant at 1 bar, with a coupling time of 2 ps, and an isothermal compressibility of 4.5×10^{-5} bar^{-1} by means of the Berendsen barostat [17]. Periodic boundary conditions were used. We set a minimal distance of 1.0 nm between the protein and the wall of each simulation box, such that two neighbours would not be closer than 2.0 nm. Water molecules (TIP3P model) and an appropriate number of counterions (necessary for the system neutrality) were added to each one of the boxes. The bonds with hydrogen atoms were constrained according to the LINCS algorithm [18]. The radius of the sphere, which defines the list for the pairwise interactions, was set to 1.0 nm. Consistently, also, the van der Waals interaction was cut off at 1.0 nm. The particle mesh Ewald method [19] for the long-range electrostatic interactions was employed using a 1.0 nm real-space cutoff. A time step of 2 fs was used to integrate the equations of motion.

The simulation procedure, which is similar to the one employed by Minicozzi and co-workers [20], is as follows: after the minimization, which was performed with the steepest descent algorithm, we equilibrated each system for 10 ns in the NVT ensemble, and for 10 ns in the NPT ensemble, at the two aforementioned temperatures. The successive production runs, at 25 and 40 °C, were 20 ns long for the PSAO and LSAO proteins, and 30 ns long for the ELAO protein.

The MD data analysis was carried out with standard GROMACS tools. The MD simulations were performed on a MARCONI100 GPU cluster at CINECA.

2.5. Protein Contact Networks Analysis

The protein contact networks (PCNs) analysis is a consolidated approach that is used to define the protein functionality on the basis of the topologies of the intramolecular interaction networks [21,22].

The method is based on the definition of the contact networks to describe the protein structure. Starting from the structural information that is embedded in the PDB files, the single-residue positions are represented as those of the corresponding alpha carbons. A link exists between a pair of residues (nodes) if their mutual distance falls in the range of 4–8 angstroms, so as to include only the relevant noncovalent intramolecular interactions.

The adjacency matrix, A, provides the mathematical description of the PCNs; its generic element, A_{ij}, is 1 if a link exists between the i-th and j-th residues (nodes), and it is 0 if otherwise. The adjacency matric properties are crucial to determining the network features, such as the node degree, which is defined as:

$$k_i = \sum_j A_{ij}$$

where the sum is extended to all the nodes (residues).

Starting from the adjacency matrix, it is possible to identify the clusters in the network that have been demonstrated to match with the functional modules in the protein structure [23].

We applied a spectral clustering algorithm [24] to identify clusters whose elements maximize the intracluster connectivity.

We adopted a twofold graphical representation of the cluster partition [23]:

1. A clustering color map: a graphical representation of the clustering matrix, whose generic element, C_{ij}, reports the number of the cluster, which is identified by the clustering algorithm, as 1 if the i-th and the j-th residues (nodes) belong to the same cluster, and as 0 if otherwise;
2. A clustering heat map projected onto ribbon protein structures; the residues belonging to the same clusters have the same colors.

Upon the network partition into clusters, it is possible to identify the clustering descriptors with specific relevance in the corresponding protein structure functionality, such as the participation coefficient, P, which is defined as follows:

$$P_i = 1 - \left(\frac{k_{si}}{k_i}\right)$$

where k_{si} is the node intracluster degree, i.e., the number of contacts of the node (residue) with the nodes belonging to the same cluster. Previous studies have demonstrated that residues with high values of the participation coefficient play a crucial role in transmitting the allosteric signal [25].

We operated all the computation in a MATLAB environment via purposed software, and for the ribbon heat maps, we used PyMol v 2.4.2.

3. Results and Discussion

3.1. LSAO and ELAO Dynamic Fluorescence Measurements

Tryptophan's light emission in the near UV (300–350 nm) is the major source of the intrinsic fluorescence in proteins [26]. The delocalized electrons of the aromatic rings of TRPs are extremely sensitive to the local environment that is produced by the protein matrix, which makes this residue a useful probe for investigating the conformational dynamics that characterize such macromolecules. In particular, lifetime and fluorescence anisotropy measurements provide general information on the structural heterogeneity and microscopic movements that occur in the nanosecond time range. The insights into the fluorescence decay of both the LSAO and ELAO samples were obtained through the phase-shift demodulation technique. The data, which are reported in Figure 1A, were analyzed by a nonlinear least squares routine, which yielded the best fit using continuous distributions of the lifetimes.

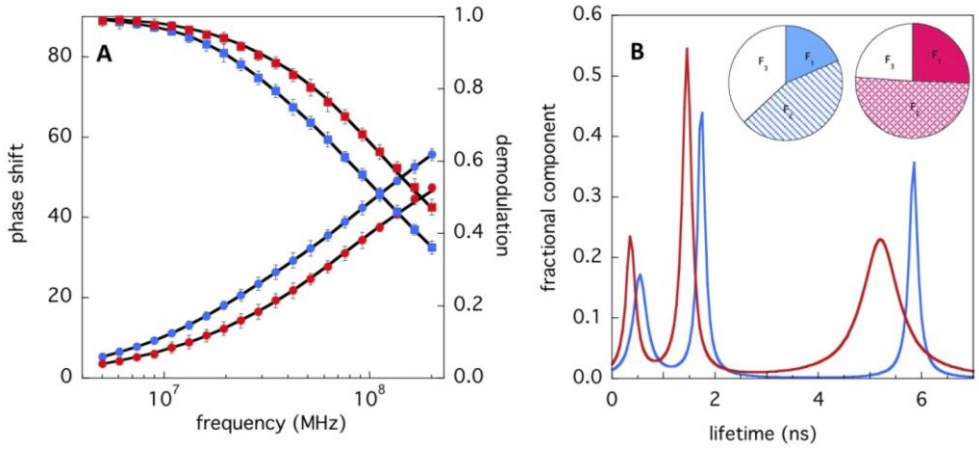

Figure 1. (**A**) Phase-shift demodulation data of ELAO (6.6 μM, blue symbols) and LSAO (7.0 μM, red symbols), as a function of the excitation frequency. The solid lines correspond to the best fit obtained on the basis of the lowest chi-squared values and residuals; (**B**) lifetime distributions corresponding to the best fit by interpolating the data of (**A**). In the inset, the relative fractional contributions of the three species (F1, F2, and F3) are reported.

The fluorescence decay is described by three main components, as is shown in Figure 1B. Such a complex heterogeneity is very common in large multitryptophan-containing proteins [27–29] and it arises from the different polarity and hydration extents that characterize the different local microenvironments of the tryptophilic residues [30]. The similarity of the two distribution profiles (Figure 1B) suggests that the two proteins share a quite similar overall tridimensional structure. However, the wider long component of the LSAO (centered at ≈ 5.2 ns, Figure 1B) indicates that, in this protein, the group of tryptophans that are characterized by the slowest dynamic fluorescence is surrounded by a more heterogeneous environment than in the ELAO. Another feature that differentiates between the fluorescence decays of the two proteins is the extent of quenching, which is more pronounced in the case of the LSAO: the phase and demodulation data are shifted to higher excitation frequencies (Figure 1A), and the corresponding data fit is characterized by shorter lifetime values (Figure 1B). Furthermore, the fractional contribution of the shorter components (F1 + F2) is larger in the case of the LSAO (Figure 1B, inset). The overall and local motilities of the two protein samples were probed by anisotropy measurements. The data, which are reported in Figure 2, required at least a double exponential fitting function, the parameters of which are reported in Table 1. For both proteins, a long component (≈60 ns) accounts for the tumbling of the whole macromolecule. In fact, the theoretical rotational correlation time of dimeric AOs is θ = 62 ns, which approximates the protein (at 25 °C) with a spherical particle, with a molecular weight of ≈ 150,000 [31]. The faster component (θ_1) is, instead, of the order of a few nanoseconds (2.7 and 3.7, respectively),

which is a time range that is too long to enable a description of the motion of the tryptophan side chains (typically from tens to hundreds of picoseconds), but that is compatible with the movements of the protein domains [26,31,32]. The smaller θ_1 value that was obtained in the case of the LSAO (Table 1), and its larger contribution to the anisotropy (F_{01}, Table 1), indicate that this protein experiences a larger local segmental mobility, with respect to the ELAO. In conclusion, three main features distinguish the LSAO intrinsic fluorescence properties from those of the ELAO: (i) A larger heterogeneity; (ii) A significant generalized quenching effect; and (iii) A greater local mobility. All of these findings strongly suggest that the matrix of the LSAO could be more hydrated than its ELAO counterpart, despite their similar tertiary structures and high-sequence homology.

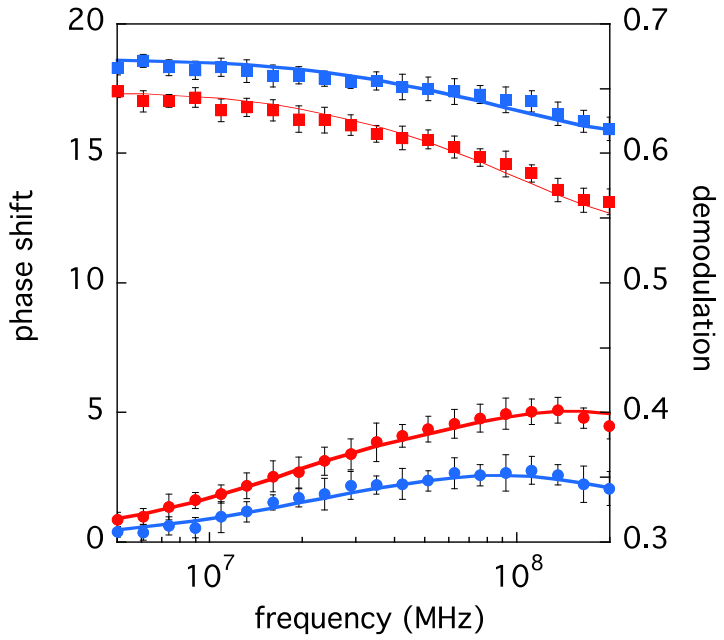

Figure 2. Fluorescence anisotropy phase-shift demodulation data of ELAO (blue symbols) and LSAO (red symbols). The parameters corresponding to the best fits (black curves) are reported in Table 1.

Table 1. Anisotropy best-fit parameters.

Sample	χ^2	θ_1 (ns)	θ_2 (ns)	F_{01}	F_{02}
ELAO	1.03	3.7 ± 0.2	61 ± 3	0.17 ± 0.01	0.11 ± 0.01
LSAO	1.00	2.7 ± 0.2	60 ± 3	0.23 ± 0.03	0.05 ± 0.02

3.2. Insights on Amine Oxidase Structural Features by In Silico Simulations and ANS Binding

Molecular dynamics were used to evaluate the possible three-dimensional structure of the ELAO and the LSAO from the available PSAO crystallographic file (see Materials and Methods). The RMSD of the backbone atom position, with respect to that of the PSAO crystallographic file, is reported in Figure 3, as a function of time, for both the ELAO and the LSAO (an in silico simulation of PSAO was also performed, as a control, and the results are reported in Figure 3).

The simulation clearly shows that the LSAO and PSAO display a similar trend, which is characterized by an initial structural relaxation ($0 < t < 7$ ns), after which the equilibrium is reached (Figure 3A,B). On the contrary, the behavior of the ELAO is more complex. In particular, at 25 °C, the first phase lasts for about 18 ns (Figure 3A), which leads to a larger average displacement ($\approx$ 0.3 nm) from the initial crystallographic model (Figure 3A). Then, in a second step, the RSMD decreases and reaches equilibrium at around $t \approx 30$ ns (Figure 3A). The simulation at $\approx$ 40 °C shows a similar trend, but with the first phase characterized by a faster relaxation time ($\approx$7 ns), and it was again followed by a small

decrease in the RSMD value (Figure 3B). These simulations suggest that the tridimensional arrangement of the ELAO might be slightly different than what is suggested by the X-ray measurements (PSAO), and from that calculated in the case of the LSAO. More insights into the ELAO's peculiar behavior can be obtained from the analysis of those descriptors that characterize the simulated protein structure and, in particular, the gyration ratio, the interchain distance, and the distance between the domains, D3–D4, which, according to the SAXS measurements, appear to be more mobile with respect to the rest of the protein [9].

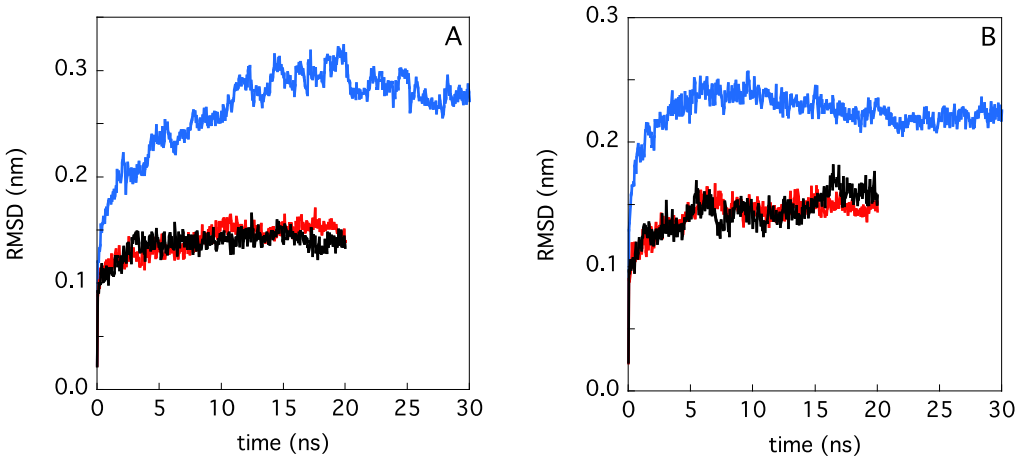

Figure 3. RMSD of the backbone atoms belonging to PSAO (black line), LSAO (red line), and ELAO (blue line), at 25 and 40 °C ((**A**) and (**B**), respectively).

The time dependencies of the abovementioned parameters are reported in Figure 4. The trends observed in the case of the LSAO are superimposable to those of the PSAO. However, the simulation for the ELAO indicates, instead, that, at equilibrium, slightly larger values are reached, which suggests a more swollen tridimensional configuration for this protein. We thus performed ANS-binding measurements as a function of the temperature on both protein samples. The interaction of the ANS with the hydrophobic patches of proteins induces a blueshift in its fluorescence spectrum. A ratiometric approach (i.e., measuring the ratio between the fluorescence intensities at two different emission wavelengths) may be useful for quantifying the hydrophobicity of the two protein surfaces and the presence of cavities. If the ELAO is indeed more swollen than the LSAO in solution, an enhanced ANS-binding capability should be expected, which is due to the presence of more accessible binding sites. The data reported in Figure 5 confirm such a hypothesis.

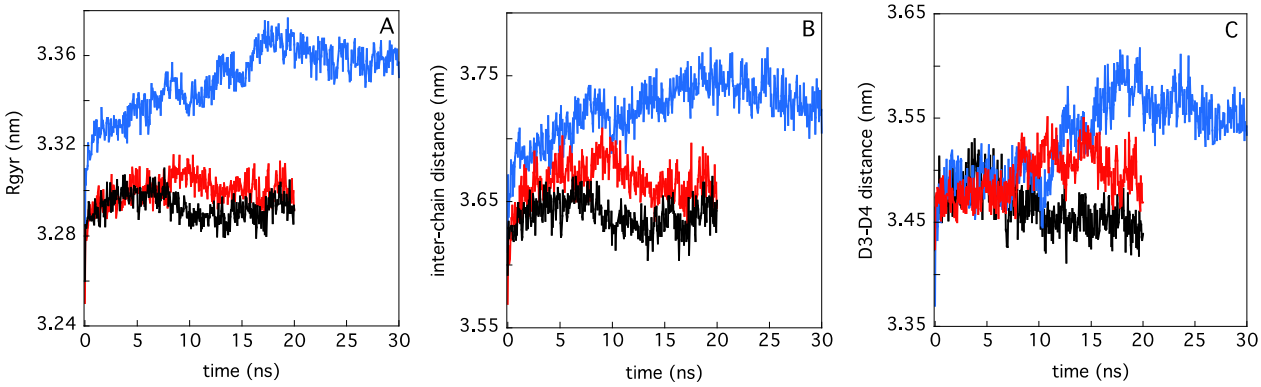

Figure 4. Radius of gyration (**A**), interchain distance (**B**), and interdomain (D3–D4) distance (**C**), of the backbone atoms belonging to PSAO (black line), LSAO (red line), and ELAO (blue line), at T = 25 °C.

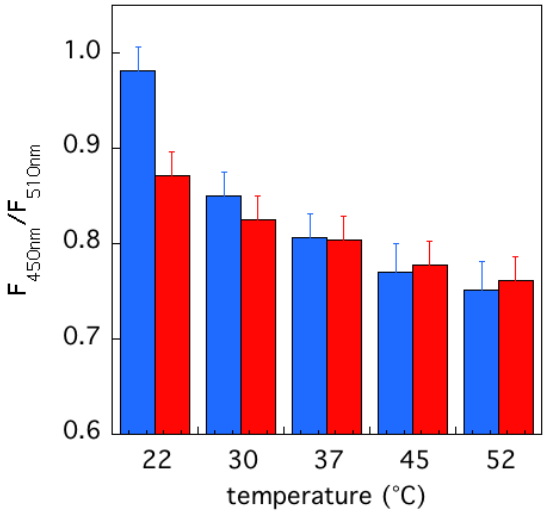

Figure 5. Ratios of ANS fluorescence intensities at two wavelengths (450 and 510 nm) as a function of temperature, in the cases of ELAO (blue bars) and LSAO (red bars). Protein and ANS concentrations were around 1 μM and 10 μM, respectively.

In fact, at room temperature (22 °C), the ratio, F_{450}/F_{510}, is 13% larger in the case of the ELAO, which demonstrates that, in this case, the ANS fluorescence spectrum is more blueshifted, which indicates a better docking to the ELAO external surface. This difference is progressively lost at higher temperatures (Figure 5), and, starting from T = 30 °C, both proteins display reduced ANS-binding capabilities. Such behavior suggests that heat might induce greater mobility, which increases the presence of water molecules in the more superficial protein cavities and pockets.

3.3. Surface and Internal Cavity Search: A Combination of Experimental and Theoretical Approaches

High pressure is a particularly suitable tool for revealing the presence of the cavities within a protein tridimensional structure. Polypeptides are not soft molecules [33,34], and their limited compressibility mainly arises from the elimination of internal voids, which is due to cavities and/or imperfections in the packing of the amino acid chains [35]. In the case of an oligomer, hydrostatic pressure can also be used to obtain information on the quaternary interactions. In fact, pressurization generally induces the reversible dissociation into monomeric species, which is a process that is strictly dependent on the presence of voids at the level of the subunit interface [36,37]. Since water penetration in a protein-buried domain strongly affects the tryptophans' spectroscopy properties, we monitored the intrinsic fluorescence of the ELAO and LSAO at increasing pressure values. As is shown in Figure 6 (insets), for both protein forms, pressurization leads to a redshift in the center of mass of the fluorescence spectrum, which is due to the progressive exposure of the buried tryptophilic residues to the solvent molecules. The change in the spectrum shape was used to quantitatively characterize the transition from 1 to 2600 atm, which obtained the curves reported in Figure 6A,B. The changes that were observed evidently correspond to a three-state transition, the first step occurring in the range of 1–1000 atm, while the second takes place between ≈1200 and ≈3000 atm (Figure 6A,B). The effects produced on both proteins are reversible, as the data obtained while restoring the initial condition (1 atm) are superimposable to those collected upon pressurization (Figure 6A,B). The persistence of a blue predominant peak (≈325 nm), even at 2500 atm (Figure 5, insets), indicates that the proteins are not fully unfolded, and that they retain a large part of their tertiary structure. On the other hand, the evident dependence of the first transition on the sample concentration (Figure 6A,B) demonstrates that the pressures induce subunit dissociation in both protein forms between 1 and 1000 atm.

Table 2. Results of the pressure-induced transition fit of the data reported in Figure 6.

Sample Concentration (μM)	χ^2	ΔG_1 (kcal M^{-1})	ΔG_2 (kcal M^{-1})	m_1 (cal/mol atm)	m_2 (cal/mol atm)	ΔV_1 (mL/mol)	ΔV_2 (mL/mol)	Y_i
[ELAO] = 0.7	0.998	11.2 ± 0.2	5.1 ± 0.1	7.2 ± 0.1	3.0 ± 0.1	≈−297	≈−123	0.38 ± 0.01
[ELAO] = 6.6	0.999	11.0 ± 0.2	4.9 ± 0.1	7.7 ± 0.3	3.1 ± 0.1	≈−318	≈−128	0.31 ± 0.01
[LSAO] = 0.8	0.997	10.4 ± 0.2	5.5 ± 0.3	3.8 ± 0.2	2.8 ± 0.2	≈−157	≈−116	0.36 ± 0.02
[LSAO] = 7.0	0.999	9.9 ± 0.2	5.5 ± 0.2	4.4 ± 0.2	3.0 ± 0.1	≈−182	≈−124	0.28 ± 0.02

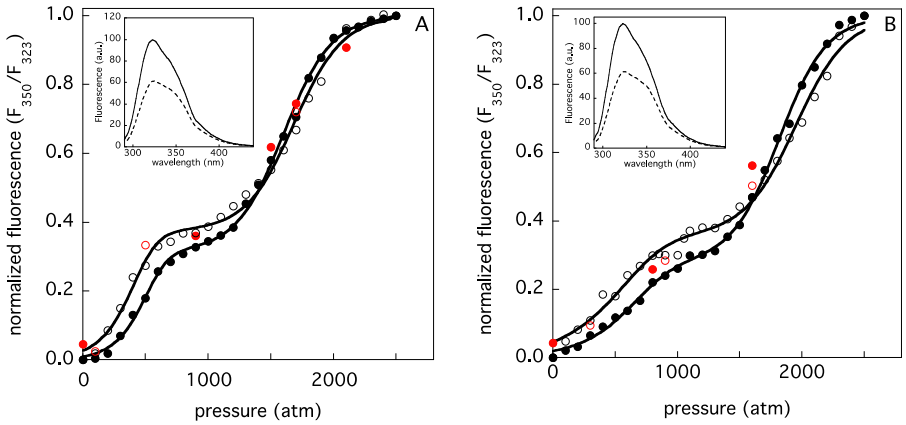

Figure 6. Pressure-induced fluorescence changes of LSAO (**A**) and ELAO (**B**), at two different concentrations (namely, 0.8 and 0.7 μM (empty symbols), and 7.0 and 6.6 μM (filled symbols), respectively). The spectral data, which normalized between 0 and 100, were obtained by measuring the ratio of the TRP fluorescence intensity observed at 350 and 323 nm (I_{350}/I_{323}). The red symbols correspond to the values obtained upon depressurization (the open and filled circles correspond, respectively, to low- and high-concentration experiments). The solid lines correspond to the best two-step fitting function, the parameters of which are reported in Table 2. In the two insets, the spectra at 1 and 2500 atm show the effects of high pressure on the shape of the protein spectrum.

On the basis of such findings, the data reported in Figure 6 were fitted according to the following scheme: $D_2 \leftrightarrow 2M \leftrightarrow 2M^*$, where D_2 is the folded dimer, and M and M* are the folded and partially unfolded monomeric species, respectively. The total free energy change is ≈ 16 kcal/mol for both proteins, two-thirds of which are ascribable to the concentration-dependent step of the transition, from 1 to 1000 bar (Table 2). In this range, the slope of the pressure-induced fluorescence change is very different in the two cases (Figure 6), and, for the ELAO, much larger values of the m_1 parameter are yielded (Table 2). This variable, m, is correlated to the change in the partial molar volume (cfr. Materials and Methods) that occurs during the protein unfolding (or the oligomer dissociation), and the conversions in mL/mol are reported in Table 2. The sign and the limited magnitude of the volume changes upon the protein pressurization (typically from a few dozen to hundred mL/mol) is generally due to the simultaneous occurrence of opposite effects, and, in particular, to: (i) A (positive) contribution, which arises from the exposure of the hydrophobic protein regions; and (ii) A (negative) change, which is due to the progressive elimination of the void spaces that are entrapped in the folded state [35,38]. Therefore, the values obtained in both the transition of the LSAO, and especially of the ELAO, suggest the presence of very large cavities, both at the subunit interface (m_1, Table 2), and within the other domains of the protein matrix (m_2, Table 2).

We thus used the frames that were obtained in the molecular dynamic simulation (Figures 3 and 4) to test such a hypothesis, and we ran two different routines (cfr. Materials and Methods) to explore the protein structure. Apart from some small- and medium-sized

pockets, three main large cavities were obtained in both cases, and their positions at the time, t = 20 ns, are shown in Figure 7A,B.

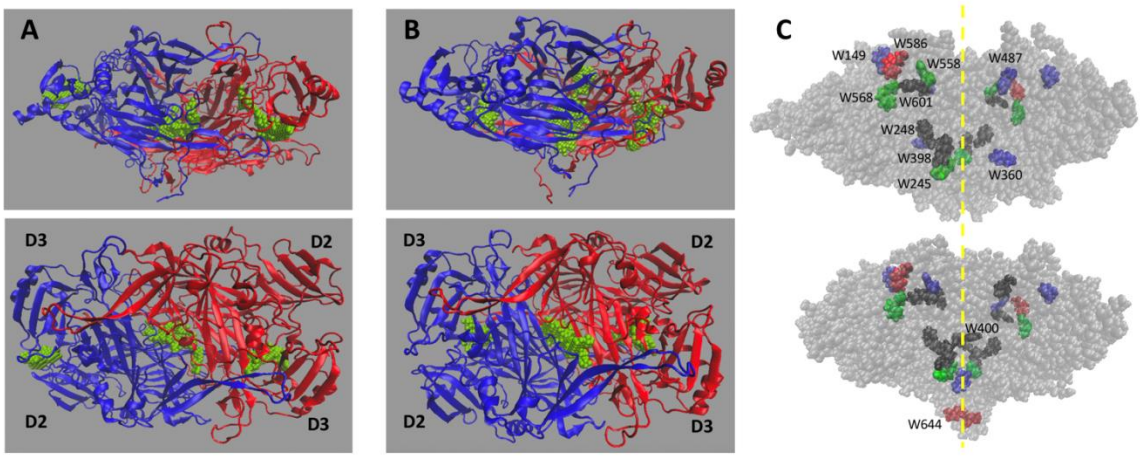

Figure 7. Side and top views: (**A**) ELAO; and (**B**) LSAO, of the three main cavity positions (green VDW spheres) found in the simulated structures at the time, t = 20 ns. The external domains, D2 and D3, are indicated in the top views. The grey structures in (**C**) report the positions of the fully buried (black), mostly buried (80% blue), buried (70%, green), and exposed (red) tryptophan residues, in the case of ELAO (top), and LSAO (bottom). The yellow dashed line indicates the position of the monomer–monomer interface.

The largest pocket is localized at the interface between the two protein subunits, in correspondence with the most deeply buried TRP residues (Figure 7C). The presence of a large cavity at the monomer–monomer interface seems to be a common feature of copper AOs [39], and it explains the origin of the first pressure-induced transition that occurs in the range of 1–1000 atm (Figure 6). In fact, subunit dissociation progressively exposes the tryptophans buried at the interface (Figure 7C), which produces a redshift in the AO's intrinsic fluorescence (Figure 6, inset). Since the theoretical size of the interface cavities in the two proteins are ≈250 and 450 Å^3, for the ELAO and LSAO, respectively, the largest volume change observed in the case of the ELAO (Table 2) represents a sort of unexpected result. A possible explanation could reside in the presence of a larger number of water molecules at the LSAO interface at 1 atm. In fact, in such a case, the volume change upon pressurization would be considerably reduced with respect to what would be observed for an emptier cavity.

Another interesting feature that emerged from the simulated files concerns the sizes and the positions of the other two cavities. As is shown in Figure 7, in the LSAO, they are situated between the external D3 domain and the large D4 domain, which forms the protein core and contains the subunit interface. A similar result was also obtained for the PSAO (data not shown). On the contrary, in the case of the ELAO, these pockets are not fully symmetric, with one cavity appearing between the domains, D2 and D3, and closer to the protein surface in one of the two subunits (Figure 7A). This finding is in line with the different time evolution that was obtained for the ELAO (Figures 3 and 4), and they suggest a greater independence among the different protein domains of the ELAO with respect to the LSAO.

3.4. Topological Characterization of AO Interfaces

We adopted a protein contact network approach in order to reach a topological characterization of the protein models that were obtained with the MD simulation and a contact network analysis. This methodology is based on a coarse-grained strategy that focuses on the carbon-α distance between the nearest-neighbor amino acids [21], and that disregards the atomic details provided by the crystallographic and simulated protein structures. Since AOs are homodimers, as a first approach, a preliminary analysis in terms of the two clusters

was attempted, and the main results of the analysis are reported in Figure 8A,B and in the clustering color map (cfr. Materials and Methods). The two main groups of amino acids, which are well recognizable in cyan and yellow, are almost coincident with the two protein subunits, in both the ELAO and the LSAO. The connectivity pattern is very symmetric for both proteins and is dominated by two relevant intersections that were observed in the blue quadrants around positions, ≈ 360 and 480 (see, for instance, the green and red arrows). Such "fringes" correspond to the amino acids that lie on the two arms that each subunit protrudes towards its mate (as is illustrated in Figure 8C,D) and that are, in fact, equivalently repeated in the rest of the clustering map (Figure 8A,B).

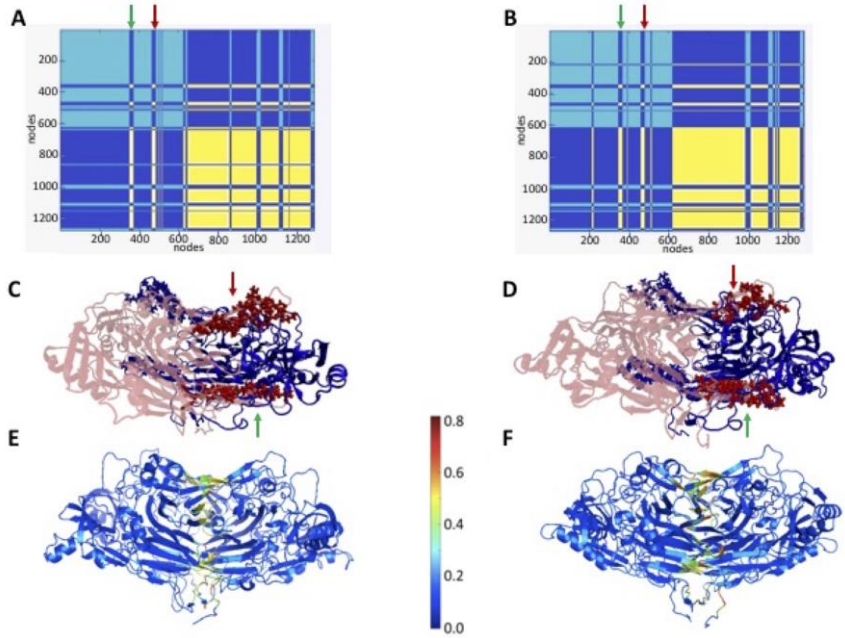

Figure 8. Topological analysis of ELAO (left) and LSAO (right) simulated structures at 20 ns using a two-cluster model. In the upper panels, the corresponding clustering color maps are reported. The background (blue) represents (i, j) residue couples that belong to different clusters, whereas the couples that pertain to the same cluster are coded with the same color (other than blue). The two axes correspond to the protein sequence. In (**C**,**D**), the residues highlighted in dark red represent those amino acids of Subunit B (light red) that are responsible of the two large intersections observed in (**A**,**B**) (green and red arrows) with Subunit A (in blue). In (**E**,**F**), the residues with the highest participation coefficient, P, are shown (i.e., the nodes of one cluster that are characterized by the largest number of contacts with residues of another cluster).

The maximum connectivity between the two subunits is, however, found at the monomer–monomer interface, as is demonstrated in Figure 8E,F by the graphic representation of the participation coefficient (p) values. This parameter assesses which nodes (residues) of one cluster are characterized by the highest number of contacts with nodes belonging to a different cluster. Overall, both the clustering maps and the p-value representations appear to be dominated by the proteins' twofold axes of symmetry. Indeed, for homodimers such as ELAO and LSAO, it is not surprising that the highest p values are found at the interface (Figure 8E,F), as long as the analysis is limited to a two-cluster model. To overcome this limitation, and to also explore the intrachain connections among the different protein domains, we therefore extended the contact network search to a larger number of clusters. The picture that emerges from such a thorough analysis is more complicated, for both proteins (Figure 9). In fact, two distinct regions per monomer may be easily visualized in the clustering patterns of both the ELAO and the LSAO: a first, compact block (including ≈200 initial residues in each subunit), and a second very large area, which ranges from the position, ≈200, to 600 (Figure 9A,B). The first group of amino acids corresponds to the

peripheral domains, D2 (6–96) and D3 (107–204), and it appears as a compact rectangular area that lies on the principal diagonal of the diagram (orange and green (Figure 9A), or cyan and orange (Figure 9B)). The presence of very few crossing fringes in this section of the representation indicates that the two peripheral domains form an almost separate entity from the rest of the protein matrix. This greater independence was already suggested by the SAXS measurements, in the case of Domain D3 [9], and it might arise from the two large cavities that separate Domains D2 and D3 from each other and/or from the cores of both proteins (Figure 7). The second large group of residues (from ≈200 to 600) is, instead, involved in an extended and capillary network of contacts (Figure 9A,B), and it is not detectable by the two-cluster analysis (Figure 8A,B). In particular, the connectivity pattern is characterized by both a few off-diagonal elements and by a large number of fringes, which lie on the main diagonal of the connectivity map.

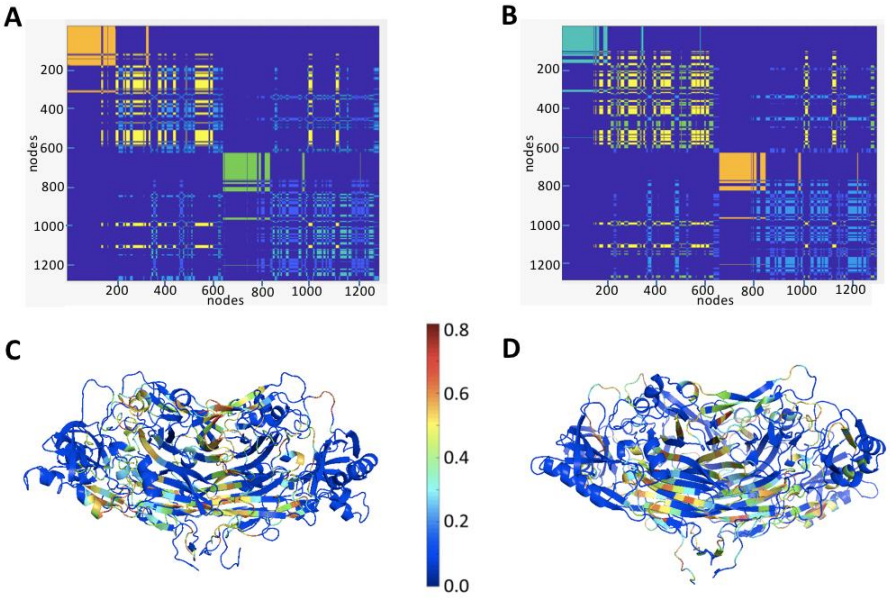

Figure 9. Topological analysis of ELAO (left) and LSAO (right) simulated structures at 20 ns using more than 2 clusters (**A**,**B**). In the lower panels (**C,D**), the graphic representations of the respective *p* values are shown.

The off-diagonal components include a series of contacts at the inter-subunit interface (from position 600 to 645), and those connections that were already detected by the two-cluster analysis (in the range of ≈350–370 and 475–485, Figure 9A,B). Overall, they are all characterized by a long-range connectivity that bridges the two monomers by a few symmetric protein segments. Indeed, for some AOs, the β-hairpin arms and the residues at the monomer–monomer interface play a major role in driving those conformational changes that allow for the communication between the two active sites [40]. At variance with the off-diagonal elements, the on-diagonal components are instead responsible for the short-range interactions among amino acids belonging to the same protein subunit. Their distributions in the two sections of the main diagonal are asymmetric (see yellow vs. cyan rectangles in each diagram in Figure 9A,B), both for the ELAO and the LSAO, which suggests that, in each protein, the two subunits adopt similar, but not identical, tridimensional conformations. The graphic rendering of the *p* values is also asymmetric, especially in the case of the ELAO (Figure 9C,D).

In conclusion, the communication between the different domains in the ELAO and LSAO seems to be ensured by both long-range and short-range interactions. While the long-range contacts between the subunits are similar and symmetric in both proteins, the asymmetry extent of the local connections appears more pronounced in the case of the ELAO (Figure 9), where the positions of the cavities are not identical in the two monomers

(Figure 7). It can be speculated that the presence of such large nonequivalent cavities might promote a "dynamic asymmetry" by facilitating local conformational changes, and by modulating the extent of the hydration in each subunit in a different way.

Despite the fact that copper amine oxidases exist as obligate dimers, a cooperation between the two equivalent active sites was found for only a few of them [41]. Furthermore, any allosteric behavior in plant AOs has been documented so far [42], and the generation of heterodimers also excludes such a possibility in bacterial AOs [43].

The structural asymmetry could provide, however, a rationale for the existence of two identical subunits in most homodimeric enzymes, as was recently reported [44,45]. According to this picture, when a subunit binds a substrate, which releases the water molecules with a negative entropy change, the other protomer compensates by a more disordered structure, which functions as an "entropy reservoir" [45]. Whether such a mechanism might also take place in amine oxidases is still a fascinating hypothesis, but a promising basis seems to exist. Studies on the asymmetry in protein oligomers are still in their infancy, but rigorous experimental data has demonstrated that, in solution, the distortion of the homomers' crystallographic structures is the rule, rather than the exception [46].

Author Contributions: E.N. and V.M. designed the experiments, interpreted the data, and contributed to the writing of the manuscript; L.D.P. designed, performed, and interpreted the contact network analysis and contributed to the writing of the manuscript; R.M. and F.P. contributed to the purification of the enzymes and to the writing of the manuscript; G.M. and A.D.V. designed the research project, designed the experiments, interpreted the data, and contributed to the writing of the manuscript. All authors have read and agreed to the published version of the manuscript.

Funding: Research was funded by Progetti di Ateneo "Beyond Borders" and "Ricerca Scientifica di Ateneo 2021–2022" of University of Rome Tor Vergata.

Institutional Review Board Statement: Not applicable.

Informed Consent Statement: Not applicable.

Conflicts of Interest: The authors declare no conflict of interest.

References

1. Levy, E.D.; Teichmann, S. Structural, evolutionary, and assembly principles of protein oligomerization. *Prog. Mol. Biol. Transl. Sci.* **2013**, *117*, 25–51. [CrossRef] [PubMed]
2. Goodsell, D.S.; Olson, A.J. Structural symmetry and protein function. *Annu. Rev. Biophys. Biomol. Struct.* **2000**, *29*, 105–153. [CrossRef] [PubMed]
3. Levy, E.D.; Pereira-Leal, J.B.; Chothia, C.; Teichmann, S.A. 3D complex: A structural classification of protein complexes. *PLoS Comput. Biol.* **2006**, *2*, e155. [CrossRef]
4. Lukatsky, D.B.; Shakhnovich, B.E.; Mintseris, J.; Shakhnovich, E.I. Structural similarity enhances interaction propensity of proteins. *J. Mol. Biol.* **2007**, *365*, 1596–1606. [CrossRef] [PubMed]
5. Swapna, L.S.; Srikeerthana, K.; Srinivasan, N. Extent of structural asymmetry in homodimeric proteins: Prevalence and relevance. *PLoS ONE* **2012**, *7*, e36688. [CrossRef]
6. Levy, E.D.; Boeri Erba, E.; Robinson, C.V.; Teichmann, S.A. Assembly reflects evolution of protein complexes. *Nature* **2008**, *453*, 1262–2655. [CrossRef]
7. Tavladoraki, P.; Cona, A.; Angelini, R. Copper-containing amine oxidases and FAD-dependent polyamine oxidases are key players in plant tissue differentiation and organ development. *Front. Plant Sci.* **2016**, *7*, 824. [CrossRef] [PubMed]
8. Kumar, V.; Dooley, D.M.; Freeman, H.C.; Guss, J.M.; Harvey, I.; McGuirl, M.A.; Wilce, M.C.; Zubak, V.M. Crystal structure of a eukaryotic (pea seedling) copper-containing amine oxidase at 2.2 A resolution. *Structure* **1996**, *4*, 943–955. [CrossRef]
9. Dainese, E.; Sabatucci, A.; Pintus, F.; Medda, R.; Angelucci, C.B.; Floris, G.; Maccarrone, M. Domain mobility as probed by small-angle X-ray scattering may account for substrate access to the active site of two copper-dependent amine oxidases. *Acta Crystallogr. D Biol. Crystallogr.* **2014**, *70 Pt 8*, 2101–2110. [CrossRef]
10. Di Venere, A.; Nicolai, E.; Rosato, N.; Rossi, A.; Finazzi Agrò, A.; Mei, G. Characterization of monomeric substates of ascorbate oxidase. *FEBS J.* **2011**, *278*, 1585–1593. [CrossRef]
11. Humphrey, W.; Dalke, A.; Schulten, K. VMD: Visual molecular dynamics. *J. Mol. Graph.* **1996**, *14*, 33–38. [CrossRef]
12. La, D.; Esquivel-Rodríguez, J.; Venkatraman, V.; Li, B.; Sael, L.; Ueng, S.; Ahrendt, S.; Kihara, D. 3D-SURFER: Software for high-throughput protein surface comparison and analysis. *Bioinformatics* **2009**, *25*, 2843–2844. [CrossRef]

13. Yu, J.; Zhou, Y.; Tanaka, I.; Yao, M. Roll: A new algorithm for the detection of protein pockets and cavities with a rolling probe sphere. *Bioinformatics* **2010**, *26*, 46–52. [CrossRef]
14. Abraham, M.J.; Murtola, T.; Schulz, R.; Pàll, S.; Smith, J.C.; Hess, B.; Lindahl, E. GROMACS: High performance molecular simulations through multi-level parallelism from laptops to supercomputers. *SoftwareX* **2015**, *1–2*, 19–25. [CrossRef]
15. MacKerell, A.D., Jr.; Feig, M.; Brooks, C.L., III. Extending the treatment of backbone energetics in protein force fields: Limitations of gas-phase quantum mechanics in reproducing protein conformational distributions in molecular dynamics simulations. *J. Comput. Chem.* **2004**, *25*, 1400–1415. [CrossRef]
16. Bussi, G.; Donadio, D.; Parrinello, M. Canonical sampling through velocity rescaling. *J. Chem. Phys.* **2007**, *126*, 014101. [CrossRef]
17. Berendsen, H.J.C.; Postma, J.P.M.; van Gunsteren, W.F.; Di Nola, A.; Haak, J.R. Molecular dynamics with coupling to an external bath. *J Chem Phys.* **1984**, *81*, 3684–3690. [CrossRef]
18. Hess, B.; Bekker, H.; Berendsen, H.J.C.; Fraaije, J.G.E.M. Lincs: A linear constraint solver for molecular simulations. *J. Comput. Chem.* **1997**, *18*, 1463–1472. [CrossRef]
19. Darden, T.; York, D.; Pedersen, L. Particle mesh ewald: An N log (N) method for ewald sums in large systems. *J. Chem. Phys.* **1993**, *98*, 10089–10092. [CrossRef]
20. Minicozzi, V.; Di Venere, A.; Nicolai, E.; Giuliani, A.; Caccuri, A.M.; Di Paola, L.; Mei, G. Non-Symmetrical Structural Behavior of a Symmetric Protein: The Case of Homo-Trimeric TRAF2 (Tumor Necrosis Factor-Receptor Associated Factor 2). *J. Biomol. Struct. Dyn.* **2021**, *39*, 319–329. [CrossRef]
21. Di Paola, L.; De Ruvo, M.; Paci, P.; Santoni, D.; Giuliani, A. Protein contact networks: An emerging paradigm in chemistry. *Chem. Rev.* **2013**, *113*, 1598–1613. [CrossRef] [PubMed]
22. Di Paola, L.; Mei, G.; Di Venere, A.; Giuliani, A. Disclosing allostery through protein contact networks. In *Allostery*; Humana: New York, NY, USA, 2021; pp. 7–20.
23. Tasdighian, S.; Di Paola, L.; De Ruvo, M.; Paci, P.; Santoni, D.; Palumbo, P.; Mei, G.; Di Venere, A.; Giuliani, A. Modules identification in protein structures: The topological and geometrical solutions. *Inf. Model.* **2014**, *54*, 159–168. [CrossRef] [PubMed]
24. Shi, J.; Malik, J. Motion segmentation and tracking using normalized cuts. In Proceedings of the Sixth International Conference on Computer Vision (IEEE Cat. No. 98CH36271), Bombay, India, 7 January 1998; Volume 1154.
25. Di Paola, L.; Giuliani, A. Protein contact network topology: A natural language for allostery. *Curr. Opin. Struct. Biol.* **2015**, *31*, 43–48. [CrossRef] [PubMed]
26. Lakowicz, J.R. Time-dependent anisotropy decays. In *Principles of Fluorescence Spectroscopy*; Kluwer Academic/Plenum Publishers: New York, NY, USA, 1999; pp. 321–346.
27. Nicolai, E.; Di Venere, A.; Rosato, N.; Rossi, A.; Finazzi Agro, A.; Mei, G. Physico-chemical properties of molten dimer ascorbate oxidase. *FEBS J.* **2006**, *273*, 5194–5204. [CrossRef] [PubMed]
28. Mei, G.; Di Venere, A.; Nicolai, E.; Angelucci, C.B.; Ivanov, I.; Sabatucci, A.; Dainese, E.; Kuhn, H.; Maccarrone, M. Structural properties of plant and mammalian lipoxygenases. Temperature-dependent conformational alterations and membrane binding ability. *Biochemistry* **2008**, *47*, 9234–9242. [CrossRef]
29. Ceccarelli, A.; Di Venere, A.; Nicolai, E.; De Luca, A.; Minicozzi, V.; Rosato, N.; Caccuri, A.M.; Mei, G. TNFR-Associated Factor-2 (TRAF2): Not Only a Trimer. *Biochemistry* **2015**, *54*, 6153–6161. [CrossRef]
30. Di Venere, A.; Nicolai, E.; Ivanov, I.; Dainese, E.; Adel, S.; Angelucci, B.C.; Kuhn, H.; Maccarrone, M.; Mei, G. Probing conformational changes in lipoxygenases upon membrane binding: Fine-tuning by the active site inhibitor ETYA. *Biochim. Biophys. Acta* **2014**, *1841*, 1–10. [CrossRef]
31. Cantor, C.R.; Schimmel, P.R. *Biophysical Chemistry. Part II*; Freeman and Company: San Francisco, CA, USA, 1980; pp. 454–465.
32. Creighton, T.E. Physical and chemical properties of soluble proteins. In *Proteins*; Freeman and Company: New York, NY, USA, 1993; pp. 268–269.
33. Howard, J. Mass, Stiffness, and Damping of Proteins. In *Mechanics of Motor Proteins and the Cytoskeleton*; Sinauer Associates Inc. Publishers: Sunderland, MA, USA, 2001; pp. 30–37.
34. Howard, J. Mechanics of the Cytoskeleton. In *Mechanics of Motor Proteins and the Cytoskeleton*; Sinauer Associates Inc. Publishers: Sunderland, MA, USA, 2001; pp. 147–148.
35. Roche, J.; Caro, J.A.; Norberto, D.R.; Barthe, P.; Roumestand, C.; Schlessman, J.L.; Garcia, A.E.; García-Moreno, B.; Royer, C.A. Cavities determine the pressure unfolding of proteins. *Proc. Natl. Acad. Sci. USA* **2012**, *109*, 6945–6950. [CrossRef]
36. Weber, G.; Drickamer, H.G. The effect of high pressure upon proteins and other biomolecules. *Q. Rev. Biophys.* **1983**, *16*, 89–112. [CrossRef]
37. Mei, G.; Di Venere, A.; Gasperi, V.; Nicolai, E.; Masuda, K.R.; Finazzi-Agrò, A.; Cravatt, B.F.; Maccarrone, M. Closing the gate to the active site: Effect of the inhibitor methoxyarachidonyl fluorophosphonate on the conformation and membrane binding of fatty acid amide hydrolase. *J. Biol. Chem.* **2007**, *282*, 3829–3836. [CrossRef]
38. Royer, C.A. Revisiting volume changes in pressure-induced protein unfolding. *Biochim. Biophys. Acta* **2002**, *1595*, 201–209. [CrossRef]
39. Wilce, M.C.; Dooley, D.M.; Freeman, H.C.; Guss, J.M.; Matsunami, H.; McIntire, W.S.; Ruggiero, C.E.; Tanizawa, K.; Yamaguchi, H. Crystal structures of the copper-containing amine oxidase from Arthrobacter globiformis in the holo and apo forms: Implications for the biogenesis of topaquinone. *Biochemistry* **1997**, *36*, 16116–16133. [CrossRef] [PubMed]

40. Takahashi, K.; Klinman, J.P. Relationship of stopped flow to steady state parameters in the dimeric copper amine oxidase from Hansenula polymorpha and the role of zinc in inhibiting activity at alternate copper-containing subunits. *Biochemistry* **2006**, *45*, 4683–4694. [CrossRef]
41. Klema, V.J.; Wilmot, C.M. The role of protein crystallography in defining the mechanisms of biogenesis and catalysis in copper amine oxidase. *Int. J. Mol. Sci.* **2012**, *13*, 5375–5405. [CrossRef]
42. Moosavi-Nejad, S.Z.; Moosavi-Movahedi, A.A.; Rezaei-Tavirani, M.; Floris, G.; Medda, R. Conformational lock and dissociative thermal inactivation of lentil seedling amine oxidase. *J. Biochem. Mol. Biol.* **2003**, *36*, 167–172. [CrossRef] [PubMed]
43. Gaule, T.G.; Smith, M.A.; Pearson, A.R.; Knowles, P.F.; McPherson, M.J. Probing the molecular mechanisms in copper amine oxidases by generating heterodimers. *Chembiochemistry* **2015**, *16*, 559–564. [CrossRef] [PubMed]
44. Kim, T.H.; Mehrabi, P.; Ren, Z.; Sljoka, A.; Ing, C.; Bezginov, A.; Ye, L.; Pomès, R.; Prosser, R.S.; Pai, E.F. The role of dimer asymmetry and protomer dynamics in enzyme catalysis. *Science* **2017**, *355*, eaag2355. [CrossRef]
45. Mehrabi, P.; Di Pietrantonio, C.; Kim, T.H.; Sljoka, A.; Taverner, K.; Ing, C.; Kruglyak, N.; Pomès, R.; Pai, E.F.; Prosser, R.S. Substrate-Based Allosteric Regulation of a Homodimeric Enzyme. *J. Am. Chem. Soc.* **2019**, *141*, 11540–11556. [CrossRef]
46. Bonjack, M.; Avnir, D. The near-symmetry of protein oligomers: NMR-derived structures. *Sci. Rep.* **2020**, *10*, 8367. [CrossRef]